ISSN: 2688-8645

Geometric Modelling and Analysis of Superelliptic Rotor Profile for Roots Vacuum Pump

Binglin Li *, Ping Luo, Manzhu Jiang

School of Mechatronic Engineering, Southwest Petroleum University, Chengdu, Sichuan, China

* Corresponding author: Binglin Li (Email: libinglin@swpu.edu.cn)

Abstract

The rotor profile has a significant influence on the performance of Roots vacuum pump. This paper proposes a novel profile which consists of a superellipse at the top and a conjugate curve at the waist. The mathematical model for the superelliptic rotor profile is established, and the constraint equations of superelliptic parameters are derived to avoid undercutting, carryover, and interference. It is found that the area utilization rate increases with the axis ratio increases when the superelliptic index is constant. In order to evaluate the pumping performance of the superelliptic rotor, three-dimensional numerical simulations are performed to analyze the pressure distribution and flow rate, and the flow fluctuation coefficient and volumetric efficiency are calculated. The results show that as the superelliptic index increases, the flow rate of the Roots pump increases, the flow fluctuation coefficient decreases, and the volumetric efficiency increases up to 88% for constant axis ratio.

Keywords

Roots Vacuum Pump; Superelliptic Rotor; Numerical Simulations; Area Utilization Rate; Flow Fluctuation; Volumetric Efficiency.

1. Introduction

Roots pump is a positive displacement vacuum pump, which has a high pumping speed and large flow rate, so it is widely used in biomedical and electronic industries. The rotor profile is directly related to the flow field distribution, pump compression ratio, volume utilization rate, and ultimate vacuum, so the rotor profile design has a crucial influence on the performance of Roots vacuum pump. It is necessary to propose a new type of rotor profile to improve the pumping performance.

Some had studied the single type curve of Roots vacuum pumps. Litvin and Feng [1] used computer to design and analyze the generated curve of cycloid gear, conjugate curve, curve curvature, singularity avoidance, which provides an important theory for the design of Roots pumps. Wang et al. [2] proposed a five-arc Roots vacuum pump, which can decease the gap between the rotor top and the chamber wall, and increase the inlet opening width, a better sealing effect is provided. Hsieh and Hwang [3-4] used high-order polynomials and sinusoidal function to express the cycloid profile equation of Roots rotor, the varied trochoid ratio can improve the area and volume efficiencies of vacuum pump. Hsieh [5] applied the elliptical cycloid to the Roots pump, the rotor profile and its undercutting equations were derived from the gear meshing theory, it was found that the smaller elliptical axial ratio can increase the discharge efficiency. Wang et al [6-7] introduced the elliptical and asymmetrical involute rotor profile, which was composed of the elliptical arc and its conjugated curve, the CFD results showed that the flow rate of the elliptical rotor were higher than that of the ordinary circular rotor, and the asymmetrical involute rotor offered an enhanced geometric flexibility and higher area-utilization ratio than involute rotor. Li et al [8] modeled and analyzed two elliptical rotor profiles separately at the apex and waist, and found that the volumetric utilization of apex elliptical rotor was higher while the pumping speed of waist elliptical rotor was faster.

Some focused on the Roots vacuum pumps with combined profiles. Kang et al [9-10] developed new rotor profiles, which were generated by three parts of circular and epicycloidal curves. The characteristic curve between pressure head versus rotational speed was analyzed numerically, and it is found that the epicycloidal profile can obtain higher performance than the traditional circular profiles. Wu and Tran [11-12] proposed a new rotor profile for multi-stage Roots pump, which was consisted of five segments: circular arc for tooth tip, variable extension epicycloid, involute, epicycloid enveloped curve, and conjugated arc for tooth root, the area utilization ratio and the meshing clearance area of different rotor profiles were calculated and compared, the incorporated geometry features provided much more design flexibility and adaptability. Li and Wang [13] proposed two types of rotor profiles consisting of arc and cycloid. The rotor profiles with the different ratio between rolling circle radius and pitch radius can increase the volume utilization rate or decrease backflow. Liu et al [14] used the arc, involute and cycloid to construct the Roots rotor profile, the gear meshing theory was used to obtain the rotor profile, which overcomes the interference and air cavitation of involute. Zhou et al [15] presented the geometry constraint method to optimize the design parameters of Roots rotor profile, the theoretical performance was assessed using the area utilization efficiency, the CFD results showed that the improvement of area utilization efficiency leads to the increase of the geometric leakage.

Some also attempted to numerically analyze the performance of rotor pump with different profiles. Houzeaux and Codina [16] divided the engagement time of two rotating tooth into multiple time steps to generate meshes, two successive time steps were related through interpolation, thus the clearance between the tooth and chamber as well as the gear meshing areas can be accurately simulated. Sun et al [17] numerically analyzed the influence of the inlet and outlet valves with two different sizes on the pressure and flow rate in Roots pumps, the velocity fields showed that the vortexes at the inlet and outlet were separately around the rotor and chamber wall. Liu et al [18] studied the effect of the rotating speed, pressure, gap on the cavitation using two-dimensional numerical model, found that the mass flow rate was larger under the cavitation condition. Additionally, the small gap size may cause the more intense cavitation, the gap size between two rotors have a greater influence on the cavitation than that between the rotor and chamber wall.

The rotor profiles of traditional design are combined by multi-segmented curves, which leads to complexities in mathematical modeling, therefore this paper proposes superelliptic profile at the top of the rotor. Firstly, the superelliptic rotor profile is modeled mathematically, and the axis ratio and superelliptic index are introduced to analyze the influence on the pumping performance. Then the numerical simulations of superelliptic rotor are performed to study the working process, pressure distribution and flow rate.

2. Superelliptic Rotor Profile Analysis

2.1. Mathematical Model of the Addendum Curves

The Roots pump with double lobe consists of two rotors arranged left and right. According to the symmetry, only a quarter of superelliptic rotor profile needs to be modeled mathematically. Half tooth curve of rotor is composed of the superelliptic arc AB and its conjugate curve BC, a and b are separately the long and short half-axes, O_1 is the rotating center, O is the superelliptic center, l is the distance OO_1, as shown in Fig.1(a). The dotted line represents the pitch circle whose radius is R, the point B is in the pitch circle, $\angle AO_1B$=45°. The superelliptic equation is expressed as:

$$\left|(x-l)/a\right|^n+\left|y/b\right|^n=1 \tag{1}$$

Where n is the superelliptic index. When $1<n<2$, the superellipse shape is similar to a rhombus; when $n=2$, it is an ellipse, especially it becomes a circle if $a=b$; when $n>2$, it is similar to a rectangle.

Fig.1(b) shows two meshing rotors which rotate in opposite directions at speeds ω_1 and ω_2. The coordinate systems S_1, S_2 and S_f are rigidly attached to the rotor axes 1, 2 and the frame, respectively. It only needs to study the superellipse curve when the parameter β is between 0 and π, and the equation of addendum curve r_1 is represented in the coordinate system S_1 as follows:

$$\mathbf{r}_1=\begin{bmatrix}x_1\\y_1\\1\end{bmatrix}=\begin{bmatrix}sgn(\cos\beta)a(sgn(\cos\beta)\cos\beta)^{2/n}+l\\b\sin^{2/n}\beta\\1\end{bmatrix} \tag{2}$$

Where $\beta\in[0,\pi/2]$ at $l<\sqrt{2}R/2$, $\beta\in[\pi/2,\pi]$ at $l>\sqrt{2}R/2$.

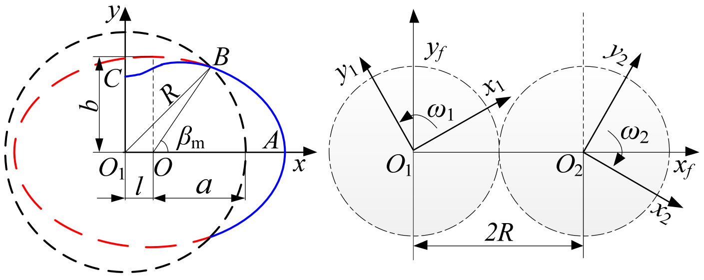

(a) (b)

Fig 1. Superelliptic rotor model

2.2. Geometric Parameters of the Rotor Profile

The coordinate of point B is $(\sqrt{2}R/2,\sqrt{2}R/2)$, the point B is substituted into the Eq.(1), b can be expressed as

$$b=\frac{\sqrt{2}R/2}{\left|1-\left[\left(\sqrt{2}R/2-l\right)/a\right]^n\right|^{1/n}} \tag{3}$$

When $l<\sqrt{2}R/2$, the point B is substituted into Eq.2, β_{m1} is given as

$$\beta_{m1}=\arctan\left(\frac{\sqrt{2}Ra/2}{b(\sqrt{2}R/2-l)}\right)^{n/2} \tag{4}$$

Where β_{m1} is the maximum value of the parameter β, $\beta\in[0, \beta_{m1}]$

When $l>\sqrt{2}R/2$, the point B is substituted into Eq.2, β_{m2} is given as

$$\beta_{m2}=-\arctan\left(-\frac{\sqrt{2}Ra/2}{b(\sqrt{2}R/2-l)}\right)^{n/2} \tag{5}$$

Where β_{m2} is the maximum value of the parameter β, $\beta\in[0, \pi+\beta_{m2}]$

2.3. Meshing Equation

According to gear meshing theory [19], the conjugate curve must satisfy the meshing equation:

$$f(\beta,\varphi)=\mathbf{n}_s\mathbf{v}_r=0 \tag{6}$$

Where φ is the rotation angle of Roots rotor, $\mathbf{n}_s$ is the normal vector of superellipse, $\mathbf{v}_r$ is the relative velocity vector. $\mathbf{n}_s$ can be expressed as:

$$\mathbf{n}_s=\frac{\partial \mathbf{r}_1}{\partial \beta}\times\mathbf{k}=(\frac{\partial x_1}{\partial \beta}\mathbf{i}+\frac{\partial y_1}{\partial \beta}\mathbf{j})\times\mathbf{k}=\frac{\partial y_1}{\partial \beta}\mathbf{i}-\frac{\partial x_1}{\partial \beta}\mathbf{j} \tag{7}$$

$\mathbf{v}_r$ is expressed as:

$$\mathbf{v}_r=v_{rx}\mathbf{i}+v_{ry}\mathbf{j}=(\boldsymbol{\omega}_1-\boldsymbol{\omega}_2)\times\mathbf{r}_1-2\boldsymbol{\omega}\times\mathbf{R} \tag{8}$$

$$\boldsymbol{\omega}_1=-\frac{\mathrm{d}\varphi}{dt}\mathbf{k} \tag{9}$$

$$\boldsymbol{\omega}_2=\frac{\mathrm{d}\varphi}{dt}\mathbf{k} \tag{10}$$

Let $\mathrm{d}\varphi/\mathrm{d}t=1$, Eqs.(9-10) are substituted into Eq.(8):

$$\mathbf{v}_r=\left[-2R\sin\varphi+2y\right]\mathbf{i}+\left[-2x+2R\cos\varphi\right]\mathbf{j} \tag{11}$$

The following meshing equation can be derived by substituting Eq.(7) and Eq.(11) into Eq.(6):

$$f(\beta,\varphi)=\left(-2\times R\times sin\varphi+2y_1\right)\times\frac{\partial y}{\partial \beta}-\left(-2\times x_1+2Rcos\varphi\right)\times\frac{\partial x}{\partial \beta}=0 \tag{12}$$

2.4. Conjugate Curve Equation

The equation of the curve $\mathbf{r}_2$ meshing with the curve $\mathbf{r}_1$ is expressed as follows:

$$\mathbf{r}_2=\mathbf{M}_{21}\mathbf{r}_1=\mathbf{M}_{2f}\mathbf{M}_{f1}\mathbf{r}_1 \tag{13}$$

$$\mathbf{M}_{2f}=\begin{bmatrix}\cos\varphi & \sin\varphi & -2R\cos\varphi\\ -\sin\varphi & \cos\varphi & 2R\sin\varphi\\ 0 & 0 & 1\end{bmatrix} \tag{14}$$

$$\mathbf{M}_{f1}=\begin{bmatrix}\cos\varphi & \sin\varphi & 0\\ -\sin\varphi & \cos\varphi & 0\\ 0 & 0 & 1\end{bmatrix} \tag{15}$$

Substituting Eqs.(14 -15) into Eq.(13)

$$\mathbf{r}_2=\begin{bmatrix}x_1\cos 2\varphi+y_1\sin 2\varphi-2R\sin\varphi\\ -x_1\sin 2\varphi+y_1\cos 2\varphi+2R\cos\varphi\\ 1\end{bmatrix} \tag{16}$$

The equation of conjugate curve $\mathbf{r}_3$ can be derived through coordinate transformation of curve $\mathbf{r}_2$:

$$\mathbf{r}_3=\begin{bmatrix}0&1&0\\-1&0&0\\0&0&1\end{bmatrix}\mathbf{r}_2=\begin{bmatrix}-x_1\sin 2\varphi+y_1\cos 2\varphi+2R\cos\varphi\\-x_1\cos 2\varphi-y_1\sin 2\varphi+2R\sin\varphi\\1\end{bmatrix}\tag{17}$$

2.5. Verification of Meshing Curve

In order to verify the accuracy of the rotor profile, the simulated trajectory diagram of the rotor rotation process is shown in Fig. 2. It can be found that the superelliptic curve and its conjugate curve mesh correctly.

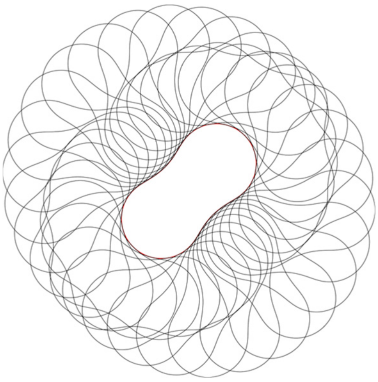

Fig 2. Verification of meshing curve

3. Profile Analysis of Superelliptic Rotor

3.1. Undercutting Analysis

The undercutting will appear when $\xi = 0$, as shown in Fig. 3. According to the meshing theory, the undercutting equation is

$$\xi_x=v_{rx}\times\frac{\partial f}{\partial\beta}-\frac{dx}{d\beta}\frac{\partial f}{\partial\varphi}=0\tag{18}$$

$$\xi_y=v_{ry}\times\frac{\partial f}{\partial\beta}-\frac{dy}{d\beta}\frac{\partial f}{\partial\varphi}=0\tag{19}$$

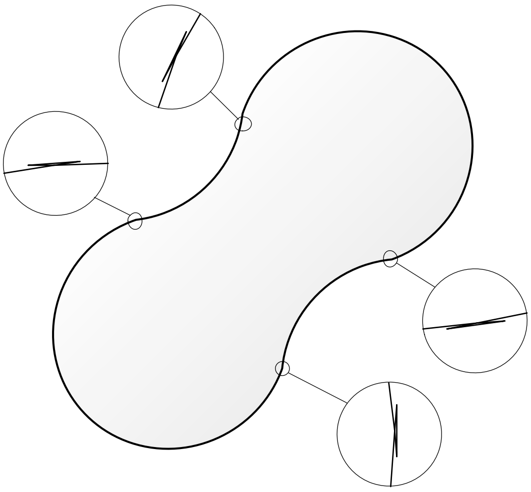

Fig 3. Undercutting of the rotor

Let $f_\beta = \dfrac{\partial f}{\partial \beta}$, $f_\varphi = \dfrac{\partial f}{\partial \varphi}$, and substituting Eq.(8) into Eqs.(18-19), the final expressions of undercutting equation are given as:

$$\xi_x = (-2R\sin\varphi + 2y)f_\beta - (-\frac{2}{n}a\left|\cos\beta\right|^{2/n-1}\sin\beta)f_\varphi = 0 \tag{20}$$

$$\xi_y = (-2x + 2R\cos\varphi)f_\beta - (\frac{2}{n}b\sin^{2/n-1}\beta\cos\beta)f_\varphi = 0 \tag{21}$$

3.2. Carryover Analysis

If the distance *d* between curvature center and coordinate origin is greater than *R*, the carryover will be occurred, as shown in Fig.4.

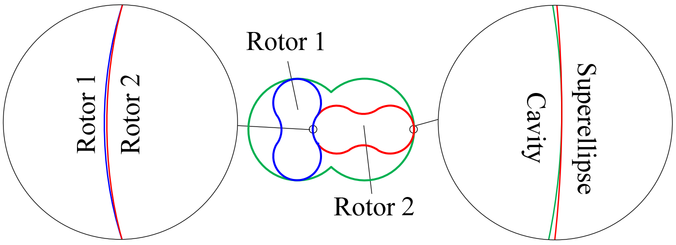

Fig 4. Carryover and interference of the rotor

The curvature can be expressed as:

$$k = \frac{\left|\mathbf{r}_1' \times \mathbf{r}_1''\right|}{\left|\mathbf{r}_1'\right|^3} \tag{22}$$

The curvature center is obtained as follows[6]:

$$\begin{cases} C_x = x_1 - \dfrac{y_1'\left[\left(x_1'\right)^2 + \left(y_1'\right)^2\right]}{y_1''x_1' - y_1'x_1''} \\ C_y = y_1 + \dfrac{x_1'\left[\left(x_1'\right)^2 + \left(y_1'\right)^2\right]}{y_1''x_1' - y_1'x''} \end{cases} \tag{23}$$

When $\beta \in [0, \pi/2]$, the curvature center is

$$k = \frac{2abn(1-1/n)\cdot\cos^{4/n-3}\beta\sin^{4/n-3}\beta}{(a^2\sin^2\beta\cos^{4/n-2}\beta + b^2\cos^2\beta\sin^{4/n-2}\beta)^{1.5}} \tag{24}$$

$$C_x = a\cos^{2/n}\beta + l - \frac{a^2\sin^2\beta\cos^{4/n-2}\beta + b^2\cos^2\beta\sin^{4/n-2}\beta}{a(n-1)\cos^{2/n-2}\beta} \tag{25}$$

$$C_y = b\sin^{2/n}\beta - \frac{a^2\sin^2\beta\cos^{4/n-2}\beta + b^2\cos^2\beta\sin^{4/n-2}\beta}{b(n-1)\sin^{2/n-2}\beta} \tag{26}$$

When $\beta \in [\pi/2, \pi]$, the curvature center is

$$k = \frac{-2abn(1-1/n)\cdot(-\cos\beta)^{2/n-1}\sin^{2/n-1}\beta\cos 2\beta}{(a^2\sin^2\beta\cos^{4/n-2}\beta + b^2\cos^2\beta\sin^{4/n-2}\beta)^{1.5}} \tag{27}$$

$$C_x = -a\cos^{2/n}\beta + l - n\frac{a^2\sin^2\beta\cos^{4/n-2}\beta + b^2\cos^2\beta\sin^{4/n-2}\beta}{a(n-1)\cos^{2/n-2}\beta} \tag{28}$$

$$C_y = b\sin^{2/n}\beta - n\frac{a^2\sin^{4-2/n}\beta\cos^{4/n-2}\beta + b^2\cos^2\beta\sin^{2/n}\beta}{b(n-1)} \tag{29}$$

The distance d can be expressed as:

$$d = \sqrt{{C_x}^2 + {C_y}^2} \tag{30}$$

3.3. Interference Analysis

When n>2, the superellipse is similar to a rectangle, and the absolute value of rotor slope near the vertex may be larger than the absolute value of arc slope of the chamber. Therefore it is necessary to avoid the interference between the rotor and the chamber when the parameter n is too large, as shown in Fig. 4.

The distance R_1 from the rotor edge to the coordinate origin is expressed as:

$$R_1 = \sqrt{x_1^2 + y_1^2} = \sqrt{(a\cos^{2/n}\beta + l)^2 + (b\sin^{2/n}\beta)^2} \tag{31}$$

The distance R_2 from the camber edge to the coordinate origin is expressed as:

$$R_2 = l + a \tag{32}$$

In order to avoid interference between the rotor and the chamber, the following condition needs to be satisfied under the condition that the maximum radius of the chamber is constant

$$R_1 \le R_2 \tag{33}$$

Substituting Eqs. (31-32) to Eq. (33) gives:

$$a^2(\cos^{4/n}\beta - 1) + 2al(\cos^{4/n}\beta - 1) + b^2\sin^{4/n}\beta \le 0 \tag{34}$$

Taylor expansion method is used to approximate:

$$\sin\beta \approx \beta \tag{35}$$

$$\cos\beta \approx 1 - \beta^2/2 \tag{36}$$

Substituting Eqs. (35-36) into Eq. (34) yields the following inequality:

$$b^2\beta^{4/n-2} \le 2a(a+l)/n \tag{37}$$

3.4. Comparative Analysis of the Parameters

In the superelliptic rotor, there are six geometrical parameters, and they are respectively the index n, the long semiaxis a , the short semiaxis b, the displacement l, the maximum radius of the rotor R_2, and the radius of pitch circle R. In order to compare, the axis ratio λ is defined as: $\lambda = a/b$.

The design parameters are selected as R_2=56mm, R=40mm. Undercutting and carryover do not occur in the superelliptic rotor only when λ ranges from 1 to 1.55 and n ranges from 2 to 2.175. Meanwhile n should be less than 2.075 to avoid the interference. Therefore, the valid range for n is from 2 to 2.075.

The area utilization rate η is given as:

$$\eta = \frac{S_c - S_r}{S_c} \tag{38}$$

where S_c, S_r is separately the area of the chamber and the rotor.

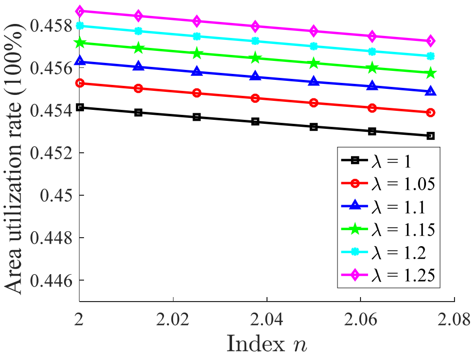

Fig 5. Area utilization rate

Fig. 5 shows the variation of area utilization rate with index *n*. It can be seen that the area utilization rate increases as the axis ratio *λ* increases when the index *n* is the same, while the area utilization rate decreases as the index *n* increases when the axis ratio *λ* is the same.

4. Working Simulation of Roots Pump

The Roots working process is numerically simulated using the Simerics MP+ software to evaluate the pumping performance of the superelliptic rotor profile, and the parameters of Roots vacuum pump are as follows: R=40mm, R_2=56mm, the rotor axial length is 120mm. The gap between two rotors is 0.2 mm, and the gap between the rotors and the chamber is 0.1 mm. The speed of the two rotors n_m is 3000 rpm.

In order to ensure the result accuracy and the computed speed, a fine mesh is generated in the region between two rotors and the chamber, and a coarse mesh is generated in the inlet and outlet. The fluid type is air, which is assumed to be an ideal gas. Simulation model selects the turbulence model. The inlet pressure is 20 kPa, the outlet pressure is 30 kPa, and the temperature is 300 K.

4.1. Independence Analysis of the Grid and Time Step

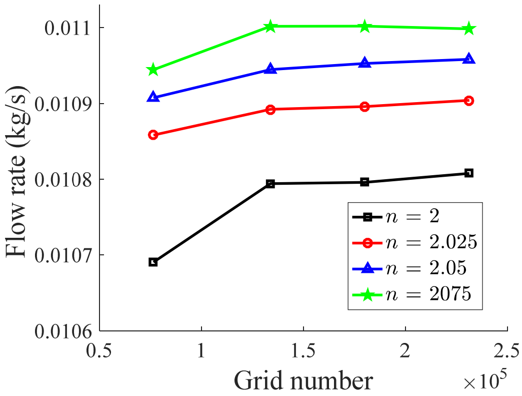

Fig 6. The gird independency

In order to verify the grid independence of the superelliptic rotor, the average flow rate of the Roots pump is obtained and compared under different grids when λ=1, as shown in Fig.6. It is found that the variation in flow rate is less than 0.2% when the grid numbers increase from 131758 to 231268. Thus the other simulations are also carried out using the 131758 grid to reduce the computed time.

On the other hand, the independence of time step is also studied, and the average flow rate is obtained and compared under different time steps when λ=1, as shown in Fig.7. It is found that the difference of flow rate is no more than 0.2% when the time steps change from 1×10^{-5} to 1×10^{-4}. So the other simulations are also carried out using the time step of 1×10^{-4} to reduce the computed time.

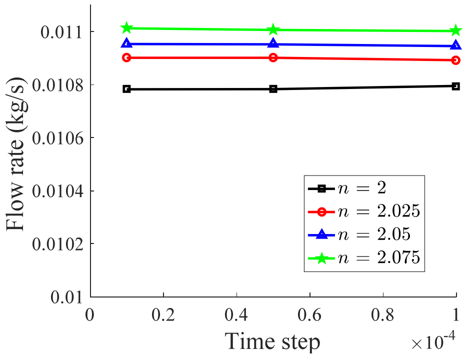

Fig 7. Time step independency

4.2. Working Process and Pressure Distribution

Fig. 8 shows the pressure distribution during the 180° rotation of the rotor with n=2, λ=1. The pressure in the chamber changes with the rotor rotation, which reflects the variation of pressure distribution in the suction, compression and exhaust of the vacuum pump.

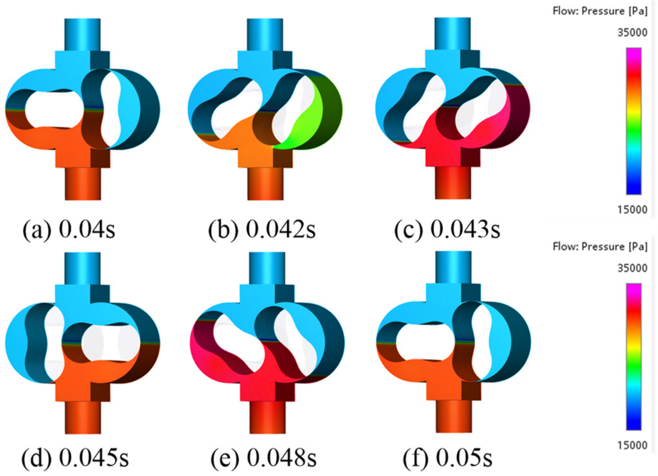

(a) 0.04s (b) 0.042s (c) 0.043s

(d) 0.045s (e) 0.048s (f) 0.05s

Fig 8. Working process pressure distribution

At 0.04s, the V_0 volume of gas from the inlet is enveloped by the right rotor, as shown in Fig. 8(a), and at this time the left rotor starts to suck. At 0.042s, the gas enveloped by the right rotor is connected to the outlet, as shown in Fig. 8(b). A fraction of the outlet gas with higher pressure will flow back, which results in the instant increase of the gas pressure in the V_0 chamber. At 0.043s, the gas enveloped by the right rotor is discharged together with the backflow gas, as shown in Fig. 8(c). At 0.045s, the left rotor also envelopes the V_0 volume of gas from the inlet, as shown in Fig. 8(d). At 0.047s, the gas enveloped by the left rotor is also connected to the outlet, while the right rotor starts to suck, as shown in Fig. 8(e). At 0.05s, the rotor has rotated 180°, and the working case shown in Fig. 8(f) is the same as the case in Fig. 8(a).

As shown in Fig.8, the working chamber is connected to the inlet during the suction stage, and the pressure in the chamber is almost identical to the inlet pressure. During the transport process, the working chamber is isolated from the inlet and outlet, and its pressure is the same as that of suction. During the discharge stage, the pressure in the working chamber suddenly increases due to the gas backflow until the pressure balance with that of the outlet. During each rotation, a total of four times V_0 volume of gas is discharged.

4.3. Flow Analysis

4.3.1. Flow Rate Comparison

The mass flow rate of the superelliptic rotor with n=2 and λ=1 is studied using the three-dimensional CFD, and the predicted results are shown in Fig.9. It can be seen that the flow rate of the vacuum pump tends to be stabile after 0.023s. To ensure data validity, the average flow rate during the third rotation is selected. It is observed that the variation of flow rate curve repeat four times sets during each rotation, which corresponds to the previous analysis that $4V_0$ volumes of the gas are discharged.

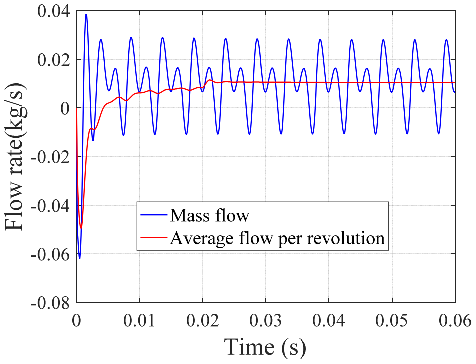

Fig 9. Mass flow rate of the superelliptic rotor profiles

The flow rate curves of the rotors with different n and λ are shown in Fig.10. It is found that the mass flow rate generally increases as n increases, and the maximum flow rate is 0.011 kg/s when n=2.075 and λ=1. The volume utilization rate decreases with the increase of n when λ is constant, and theoretically the flow rate should also reduce, but the predicted flow rate increases due to the influence of backflow. The top profile of superelliptic rotor becomes wider as the index n increases as shown in Fig.11, in other words the curvature of the rotor top profile becomes larger, which increases the clearance flow resistance between the rotor and the chamber, as a result of the decrease of backflow and leakage, and the increase of the compression ratio. Thus the pumping performance is improved.

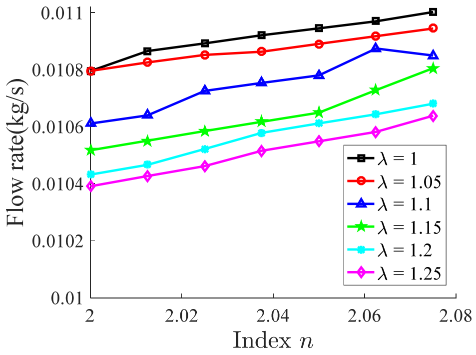

Fig 10. Flow rate

As observed from Fig.10, the flow rate of *n*=2.075 is lower than that of *n*=2.0625 when *λ*=1.1, which may be because the influence of volume utilization rate on the flow rate is greater than that of backflow, consequently it leads to the decrease of the flow rate.

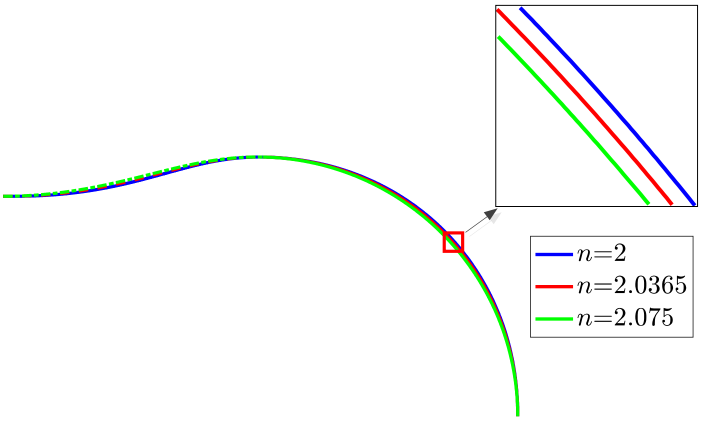

Fig 11. The superellipse rotor profile

4.3.2. Flow Fluctuation

The fluctuation coefficient of flow rate *σ* is defined as a performance index related to vibration and noise [7], its expression is given as:

$$\sigma = \frac{P_{max} - P_{min}}{P} \tag{39}$$

As shown in Fig. 12, the fluctuation coefficient decreases with increase of the index *n* when *λ* is constant, this indicates that increasing the index *n* can enhance the discharge efficiency and decrease the vibration and noise.

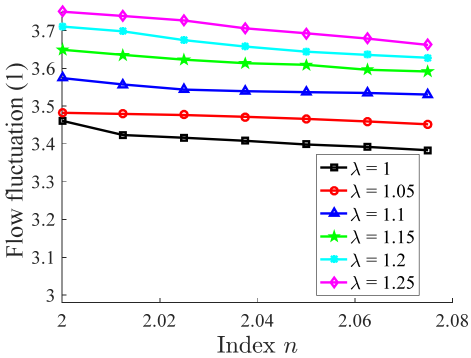

Fig 12. Flow fluctuation coefficient

4.3.3. Volumetric Efficiency

The theoretical flow rate Q_t is expressed as:

$$Q_t = \rho_i \cdot V_r \cdot \frac{n_m}{60} \tag{40}$$

where ρ_i is the density of the ideal gas under the inlet pressure and temperature condition, it can be calculated according to the state equation of ideal gas, V_r is the suction volume per rotation, it can be obtained as:

$$V_r = 2L\eta\pi R_2^{\,2} \tag{41}$$

The volumetric efficiency of Roots pump is the ratio of the actual flow rate to the theoretical flow rate at the outlet, it can be expressed as:

$$\kappa = \frac{Q_a}{Q_t} \times 100\% \tag{42}$$

The volumetric efficiencies of rotors with different parameters are shown in Fig.13. The volumetric efficiency increases with the increase of the index *n* when the axis ratio *λ* is constant, and decreases with the increase of the axis ratio *λ* when the index *n* is constant. The maximum volumetric efficiency is 88%, which indicates that the results of numerical simulation are reliable.

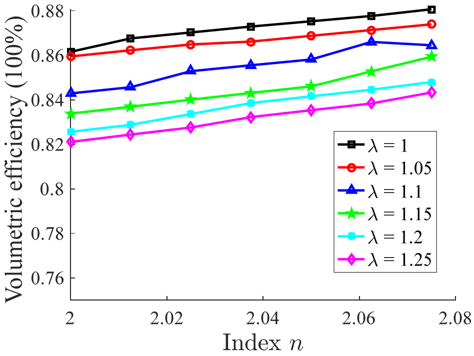

Fig 13. Volumetric efficiency

5. Conclusion

This paper proposes a new Roots vacuum pump with superelliptic rotor profile, and the profile equation is modeled mathematically, the undercutting, carryover, and interference are analyzed by taking into account the constraint conditions, and three-dimensional CFD is performed to study the pumping performance. Some conclusions are obtained as follows:

Compared with traditional circular arc rotors, the superelliptic rotor has more independent parameters of geometric design, and the superelliptic rotor for the special conditions of *λ*=1 and *n*=2 becomes the circular arc rotor.

The area utilization rate increases with the increase of the axis ratio *λ* when the index *n* is constant, and decreases with the increase of the index *n* when the axis ratio *λ* is constant. The theoretical flow rate also increases when the area utilization rate increases. The compression ratio of superelliptic rotor is higher than that of circular arc rotor.

The results of numerical simulation show that the predicted flow rate of the superelliptic rotor generally increases with the increase of index *n*, the fluctuation coefficient of flow rate *σ* decreases with the increase of the index *n*, and the volumetric efficiency increases with the increase of the index *n*, and the maximum volumetric efficiency can reach 88% when the axis ratio *λ* is constant. The superelliptic rotor has a better pumping performance when the axis ratio *λ*=1 and the index *n*=2.075.

References

[1] F.L. Litvin, P. H. Feng, Computerized design and generation of cycloidal gearings. Mech. and Mach. Theory 31(7) (1996) 891-911.

[2] P.Y. Wang, Z.H. Fong, H.S. Fang. Design constraints of five-arc Roots vacuum pumps. Proc. Instit. Mech. Eng. Part C 216(2) (2002) 225-234.

[3] C.F. Hsieh, Y.W. Hwang. Tooth profile of a Roots rotor with a variable trochoid ratio. Math. Comput. Model. 48(1-2) (2008) 19-33.

[4] Y.W. Hwang, C.F. Hsieh. Study on high volumetric efficiency of the Roots rotor profile with variable trochoid ratio. Proc. Instit. Mech. Eng. Part C 220(9) (2006) 1375-1384.

[5] C.F. Hsieh. A new curve for application to the rotor profile of rotary lobe pumps. Mech. Mach. Theory 87 (2015) 70-81.

[6] J. Wang, R. Liu, S. Yang, et al. Geometric study and simulation of an elliptical rotor profile for Roots vacuum pumps. Vacuum. 153 (2018) 168-175.

[7] J. Wang, S. Yang, R. Sha, et al. Geometric design and analysis of novel asymmetrical rotors for Roots vacuum pumps. J. Mech. Des. 142(6) (2020) 064501.

[8] Z. Li, X. Wang, X. Han, et al. Geometric design of two novel rotor profiles for Roots vacuum pumps with elliptical curve. Results Eng. 25 (2025) 104170.

[9] Y.H. Kang, H.H. Vu. A newly developed rotor profile for lobe pumps: Generation and numerical performance assessment, J. Mech. Sci. Technol. 28 (2014) 915-926.

[10] Y.H. Kang, H.H. Vu, C.H. Hsu. Factors impacting on performance of lobe pumps: A numerical evaluation, J. Mech. 28(2) (2012) 229-238.

[11] Y.R. Wu, V.T. Tran. Generation method for a novel Roots rotor profile to improve performance of dry multi-stage vacuum pumps. Mech. Mach. Theory 128 (2018) 475-491.

[12] V.T. Tran, B.T. Thanh, B.T. Long, et al. Study on the effects of tooth profile design parameters of rotor to performance of vacuum pump. Int. J. Mod. Phys. 34(22n24) (2020) 2040141.

[13] Z.Q. Li, X.J. Wang. New cycloid rotor profiles design under different rolling circle radii for Roots vacuum pumps. SN Appl. Sci. 4(10) (2022) 280.

[14] L. Liu, P. Chen, J. Du. Design of rotor profile of a new roots vacuum pump. J. Phys: Conf. Ser 1676(1) (2020) 012078.

[15] S. Zhou, X. Jia, X. Peng, et al. The effects of design parameters on performance of a novel roots profile. Int. J. Hydrog. Energy 48(6) (2023) 2368-2384.

[16] G. Houzeaux, R. Codina. A finite element method for the solution of rotary pumps. Comput. Fluids 36(4) (2007) 667-679.

[17] S.K. Sun, B. Zhao, X.H. Jia, et al. Three-dimensional numerical simulation and experimental validation of flows in working chambers and inlet/outlet pockets of Roots pump. Vacuum 137 (2017) 195-204.

[18] Y. Liu, L. Wang, Z. Zhu. Numerical study on flow characteristics of rotor pumps including cavitation. Proc. Instit. Mech. Eng. Part C 229(14) (2015) 2626-2638.

[19] F.L. Litvin, A. Fuentes. Gear geometry and applied theory. Cambridge university press, 2004.